

# Ferro-Pyro-Phototronic Effect in Monocrystalline 2D Ferroelectric Perovskite for High-Sensitive, Self-Powered, and Stable Ultraviolet Photodetector

Linjuan Guo, Xiu Liu, Linjie Gao, Xinzhan Wang, Lei Zhao, Wei Zhang, Shufang Wang,\* Caofeng Pan,\* and Zheng Yang\*



Cite This: *ACS Nano* 2022, 16, 1280–1290



Read Online

ACCESS |



Metrics & More



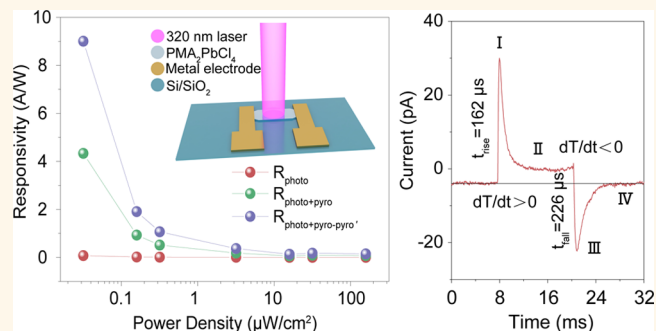
Article Recommendations



Supporting Information

**ABSTRACT:** 2D hybrid perovskite ferroelectrics have drawn great attention in the field of photodetection, because the spontaneous polarization-induced built-in electric field can separate electron-hole pairs, and makes self-powered photodetection possible. However, most of the 2D hybrid perovskite-based photodetectors focused on the detection of visible light, and only a few reports realized the self-powered and sensitive ultraviolet (UV) detection using wide bandgap hybrid perovskites. Here, 2D ferroelectric PMA<sub>2</sub>PbCl<sub>4</sub> monocrystalline microbelt (MMB)-based PDs are demonstrated. By using the ferro-pyro-phototronic effect, the self-powered Ag/Bi/2D PMA<sub>2</sub>PbCl<sub>4</sub> MMB/Bi/Ag PDs show a high photoresponsivity up to 9 A/W under 320 nm laser illumination, which is much higher than those of previously reported self-powered UV PDs. Compared with responsivity induced by the photovoltaic effect, the responsivity induced by the ferro-pyro-phototronic effect is 128 times larger. The self-powered PD also shows fast response and recovery speed, with the rise time and fall time of 162 and 226 μs, respectively. More importantly, the 2D PMA<sub>2</sub>PbCl<sub>4</sub> MMB-based PDs with Bi/Ag electrode exhibit significant stability when subjected to high humidity, continuous laser illumination, and thermal conditions. Our findings would shed light on the ferro-pyro-phototronic-effect-based devices, and provide a good method for high-performance UV detection.

**KEYWORDS:** ferro-pyro-phototronic effect, 2D ferroelectric perovskites, monocrystalline, self-powered, UV photodetectors



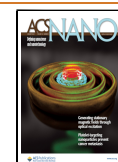
Due to high anti-interference ability, ultraviolet (UV) photodetection technology has potential applications in military detection, environmental monitoring, flame warning, life science, and astronautics.<sup>1–5</sup> In particular, the wide bandgap semiconductor-based UV photodetectors (PDs) have shown the advantages of simple structure, easy miniaturization, and good robustness for radiation and severe environments. Nowadays, the UV PDs are mainly based on traditional wide-bandgap semiconductors like GaN, ZnO, and Ga<sub>2</sub>O<sub>3</sub>, which usually need expensive production equipment.<sup>6–9</sup> Very recently, hybrid perovskites have drawn much attention in high-efficiency solar cells,<sup>10–12</sup> PDs,<sup>13–16</sup> lasers,<sup>17,18</sup> and light-emitting diodes,<sup>19,20</sup> due to their excellent optoelectronic properties, such as large light absorption coefficient, high carrier mobility, long carrier diffusion length, low trap density, and tunable bandgap. A recent advance has demonstrated perovskite-based PD with a responsivity of  $1.5 \times$

$10^4$  A/W and a detectivity exceeding  $7 \times 10^{15}$  Jones.<sup>14</sup> However, up to date, most of the perovskite-based PDs focused on the detection of visible light, and only a few reports realized the sensitive detection of UV light using wide bandgap hybrid perovskites.<sup>21–26</sup> Moreover, most of the above works need an external bias, increasing the cost and complexity. Therefore, the realization of self-powered and sensitive UV detection based on wide-bandgap hybrid perovskites is in urgent need.

Received: October 15, 2021

Accepted: January 5, 2022

Published: January 7, 2022



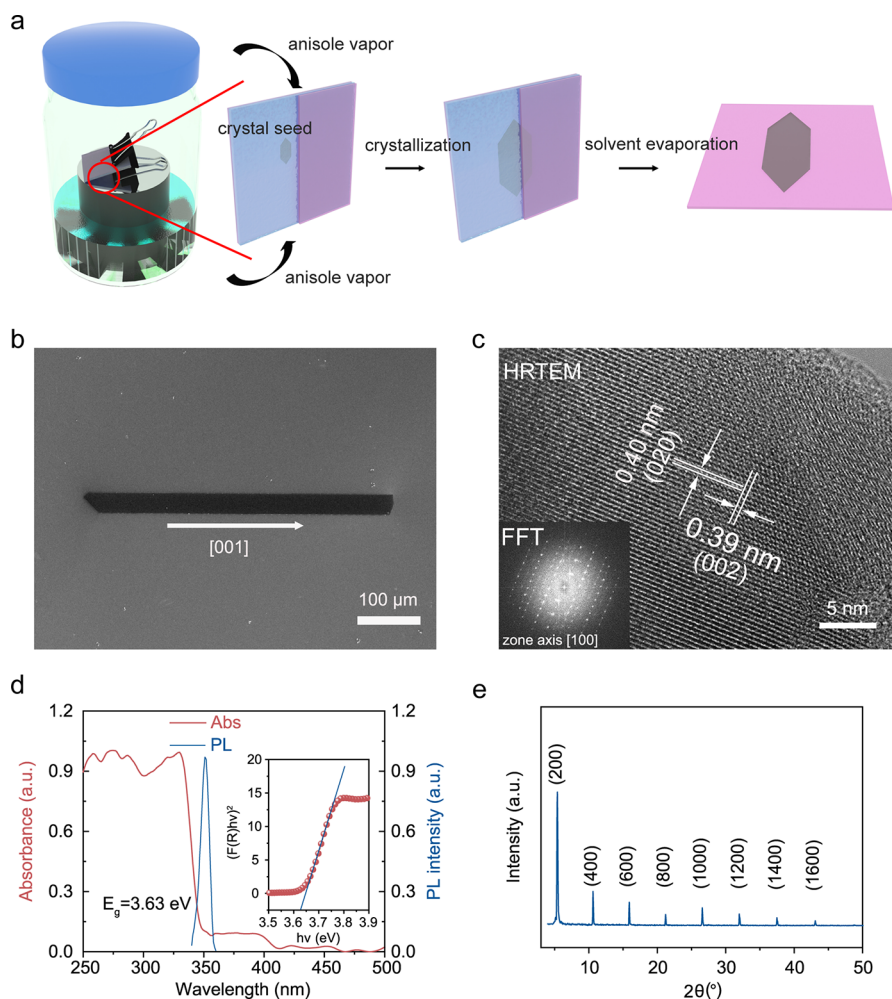


**Figure 1.** SCAAS growth process, structural, and optical properties of 2D PMA<sub>2</sub>PbCl<sub>4</sub> MMB. (a) Schematic diagram of SCAAS growth process to grow PMA<sub>2</sub>PbCl<sub>4</sub> MMB. (b) SEM image and (c) HRTEM image of a PMA<sub>2</sub>PbCl<sub>4</sub> MMB, the inset is the corresponding SAED patterns of 2D PMA<sub>2</sub>PbCl<sub>4</sub> MMB. (d) The absorbance spectrum and PL spectrum of the PMA<sub>2</sub>PbCl<sub>4</sub> MMB. The inset is the corresponding Tauc plot of the PMA<sub>2</sub>PbCl<sub>4</sub> MMB, showing a bandgap of 3.63 eV. (e) XRD patterns of the PMA<sub>2</sub>PbCl<sub>4</sub> MMB.

Construction of *p-i-n* solar cell structure<sup>27,28</sup> or integrating PDs with an energy harvester unit<sup>29</sup> are two common methods to realize self-powered photodetection, increasing the device cost and weight. Recently, ferroelectric effect has shown its potential in self-powered PDs because spontaneous polarization in ferroelectric semiconductors can separate electron-hole pairs.<sup>30,31</sup> As an important dielectric property, ferroelectricity is often observed in some 2D layered perovskites, such as (benzylammonium)<sub>2</sub>PbCl<sub>4</sub> (PMA<sub>2</sub>PbCl<sub>4</sub>),<sup>32</sup> (butylamine)<sub>2</sub>PbCl<sub>4</sub>,<sup>33</sup> and (butylamine)<sub>2</sub>CsPb<sub>2</sub>Br<sub>7</sub>.<sup>34</sup> Typically, the ferroelectric PMA<sub>2</sub>PbCl<sub>4</sub>, a wide band gap semiconductor (3.65 eV), consists of the infinite layers of corner-sharing PbCl<sub>6</sub> octahedra interleaved by benzylammonium cations.<sup>32</sup> Since all the benzylammonium cations show a relatively ordered state, in which the C–N bonds of benzylammonium cations align along the *c* axis, so that the spontaneous polarization direction is along the *c* axis. Since ferroelectricity is a subset of pyroelectricity, thus all ferroelectric materials belong to pyroelectric materials. Therefore, pyroelectric effects can also be utilized to enhance the PDs' performance based on ferroelectric materials.

Recently, by utilizing the light-induced pyro-phototronic effect, a three-way coupling effect among pyroelectricity, photoexcitation, and semiconductor, the photodetection

performances of the ZnO/Si,<sup>35</sup> the CdS/Si,<sup>36</sup> the CdS/SnS<sup>37</sup> heterojunctions, and ZnO/Ag Schottky junctions<sup>38</sup> are greatly improved. Furthermore, Yang coupled pyroelectric and photovoltaic effects in ferroelectric materials BaTiO<sub>3</sub>, and a ferro-pyro-phototronic effect had been utilized to enhance the photoresponses of ITO/BaTiO<sub>3</sub>/Ag.<sup>39</sup> The change of spontaneous polarization derived from light-induced thermal fluctuation can effectively modulate the carrier generation, separation, transportation, and recombination at the interface of the junctions. Therefore, responsivity, detectivity, and response/recovery speed of PDs utilizing the pyro-phototronic effect can be significantly enhanced, and self-powered photodetection can also be realized. In our previous work, the pyro-phototronic effect was introduced to boost the MAPbI<sub>3</sub> single film/Si *p-n* junction-based broadband PDs' performance.<sup>40</sup> Utilizing the ferro-pyro-phototronic effect in wide bandgap 2D ferroelectric perovskite will be a potential approach for self-powered and sensitive UV light detection.

Besides, stability is another critical issue that hinders the practical applications of PDs based on metal halide perovskites. Traditional metal halide perovskites-based PDs usually use metals, typically Au, as the electrode to form metal–semiconductor–metal (M–S–M) structure. However, the reactions between the metal electrodes and halogens from

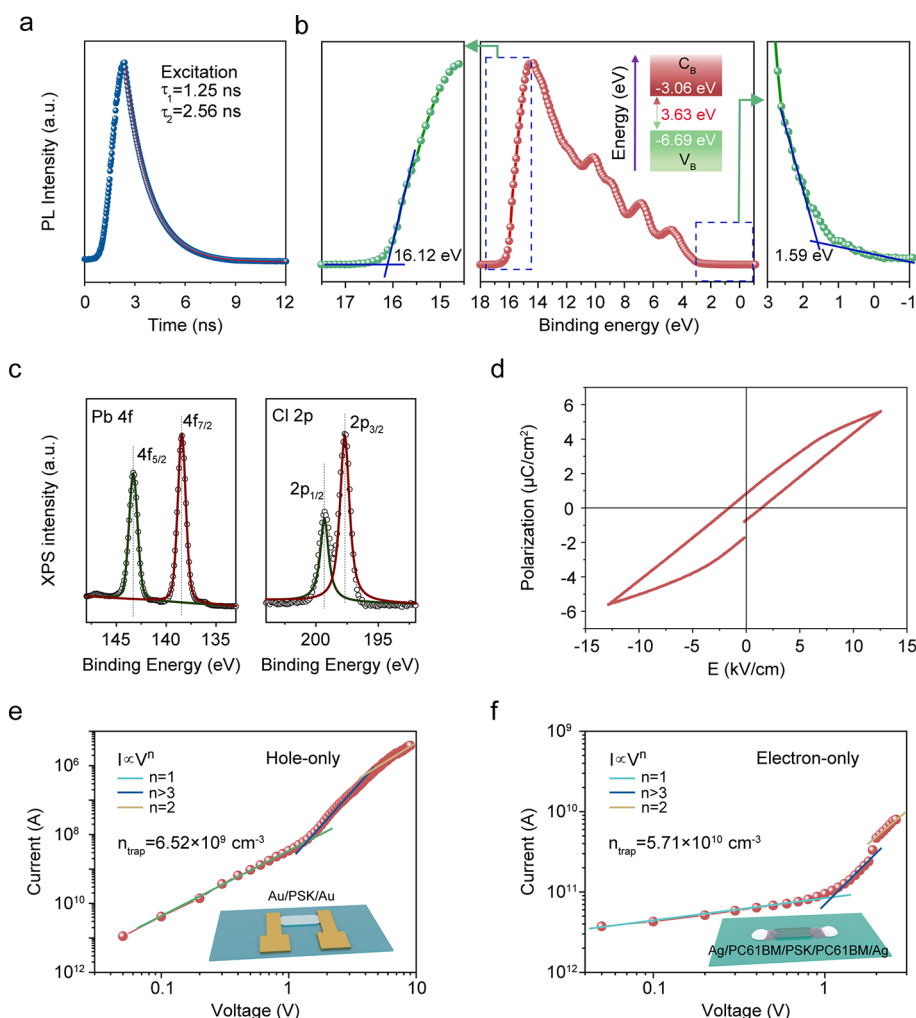


**Figure 2.** Optical and semiconductor properties of the 2D PMA<sub>2</sub>PbCl<sub>4</sub> MMB. (a) TRPL of the 2D PMA<sub>2</sub>PbCl<sub>4</sub> MMB at 275 nm. (b) UPS of the 2D PMA<sub>2</sub>PbCl<sub>4</sub> MMB. The inset is an energy band diagram for the 2D PMA<sub>2</sub>PbCl<sub>4</sub> MMB. (c) XPS spectra of Pb 4f and Cl 2p for PMA<sub>2</sub>PbCl<sub>4</sub> MMB. (d)  $P$ - $E$  hysteresis loop of PMA<sub>2</sub>PbCl<sub>4</sub> MMB.  $I$ - $V$  curves of the (e) hole-only and (f) electron-only 2D PMA<sub>2</sub>PbCl<sub>4</sub> MMB devices.

the perovskites during prolonged operation are inevitable,<sup>41,42</sup> which will lead to the degradation of photodetection performances. Recently, a bismuth (Bi) layer was reported to act as a robust permeation barrier that could protect the metal electrode from haloid corrosion,<sup>43</sup> while maintaining the devices' performances. Therefore, Bi is an ideal electrode to form an M-S-M structure for high-stable PDs.

In this work, 2D ferroelectric PMA<sub>2</sub>PbCl<sub>4</sub> monocrystalline microbelts (MMBs) with well-controlled orientation and good crystallinity were obtained by space-confined assisted antisolvent growth method. Then, the PMA<sub>2</sub>PbCl<sub>4</sub> MMB was fabricated into a self-powered UV PD by simply depositing the Bi/Ag electrode onto two ends of the MMB. This self-powered UV PDs show excellent photodetection performance, including a low dark current of  $7.52 \times 10^{-12}$  A, a high responsivity ( $R$ ) of 9 A/W, and a fast response speed (162 μs), which should be attributed to the ferro-pyro-phototronic effect in 2D ferroelectric PMA<sub>2</sub>PbCl<sub>4</sub> MMB. Furthermore, the PDs with Bi interlayer electrode display more favorable antihumidity, illumination resistant, and thermal stability than the devices with Au electrode. Our unencapsulated device retains 71.6% of initial response after being stored in  $70 \pm 10\%$  humidity for 30 days. Our work will provide a good method of coupling ferro-

pyro-phototronic effect on prominent optoelectronic devices made from 2D ferroelectric perovskites.

## RESULTS

Here, the space-confined assisted antisolvent (SCAAS) growth method is used to prepare PMA<sub>2</sub>PbCl<sub>4</sub> MMB with the well-controlled thickness (Figure 1a). The detailed growth procedure can be seen in the Methods section. The precursor solution was confined in two Si/SiO<sub>2</sub> slices with space limited to a micrometer scale. Nontoxic and greener solvent anisole was used as the antisolvent. With the diffusion of anisole vapors into precursor solution, the MMBs with controlled orientation would be grown onto the Si/SiO<sub>2</sub> slices after 48 hours growth. Figure 1b, Supporting Information (SI) Figure S1a,b show a scanning electron microscope (SEM) image, an enlarged SEM image, and photograph of a typical PMA<sub>2</sub>PbCl<sub>4</sub> MMB grown on the Si/SiO<sub>2</sub> substrate with a length of more than 500 μm, a width of 30–50 μm and  $c$ -axis along [001] orientation, respectively. All the MMBs exhibit smooth surfaces, regular shapes, and sharp edges, indicating the monocrystalline nature. With applying a large pressure (~150 kPa), the height can be controlled by less than 1 μm. SI Figure S1c shows the thickness distribution of the

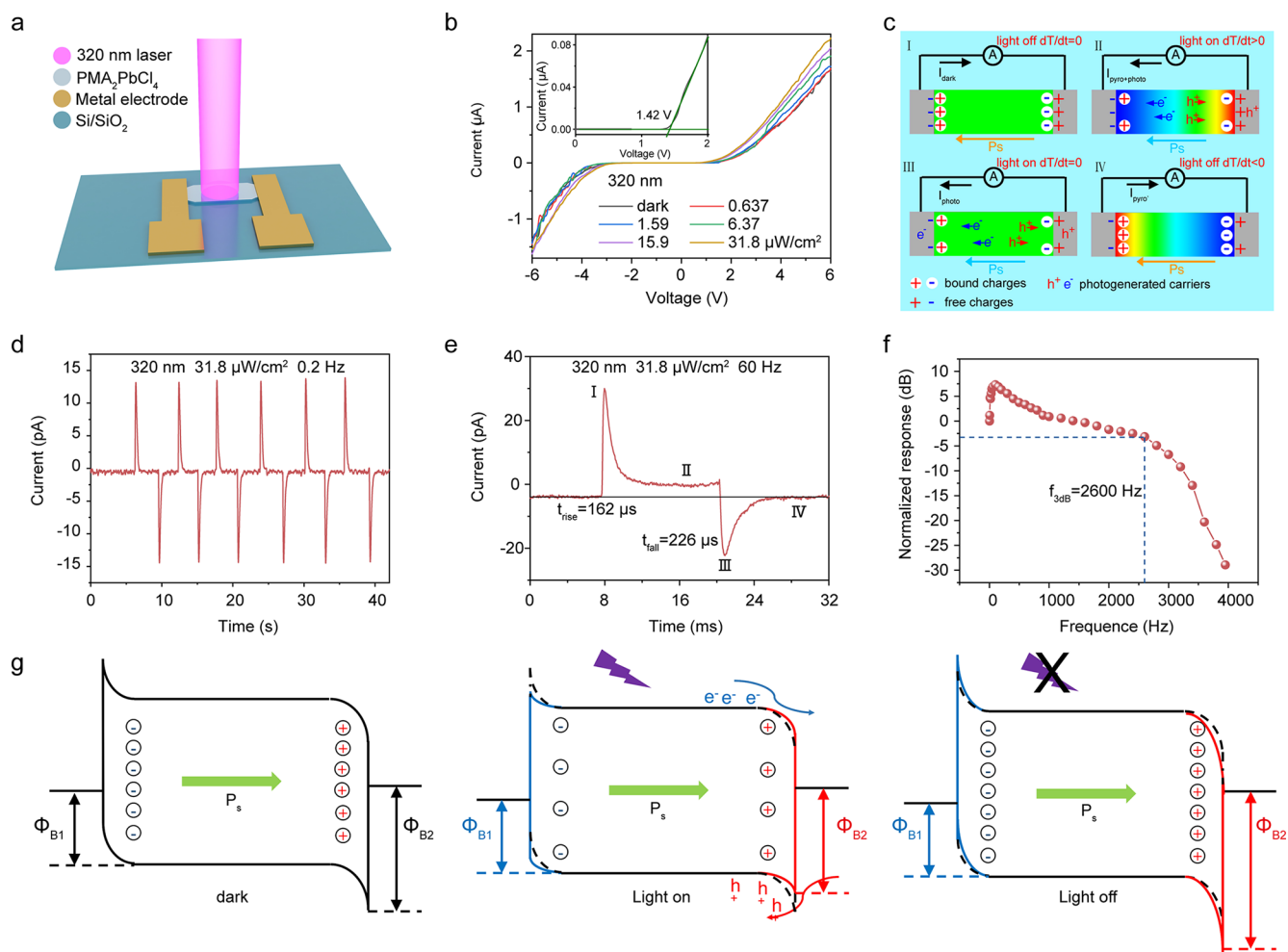


**Figure 3.** Performance and working mechanism of the Ag/Bi/2D PMA<sub>2</sub>PbCl<sub>4</sub> MMB/Bi/Ag PDs. (a) Schematic illustration of the 2D PMA<sub>2</sub>PbCl<sub>4</sub> MMB-based PDs on Si/SiO<sub>2</sub> substrate. (b) *I*–*V* curves of the PMA<sub>2</sub>PbCl<sub>4</sub> MMB-based PD under dark and 320 nm laser illumination with different power densities, the inset is the corresponding enlarging the *I*–*V* curve under dark condition. (c) Schematic working mechanism of the ferro-pyro-phototronic effect of the PD as turning on and turning off the laser. (d) Photoreponse behavior of the self-powered PD under 320 nm laser illumination with the power density of 31.8 μW/cm<sup>2</sup> under zero bias at a frequency of 0.2 Hz. (e) Temporal photocurrent response of the PMA<sub>2</sub>PbCl<sub>4</sub> MMB-based PD under 320 nm laser illumination with a power density of 31.8 μW/cm<sup>2</sup> under zero bias at 60 Hz. (f) Frequency response of the PMA<sub>2</sub>PbCl<sub>4</sub> MMB PD. (g) Energy band diagrams of the PD in different conditions.

PMA<sub>2</sub>PbCl<sub>4</sub> MMBs obtained by step profiler with an average thickness of 482 ± 17 nm. The thickness distribution of a typical PMA<sub>2</sub>PbCl<sub>4</sub> MMB is shown in SI Figure S1d. The high-resolution transmission electron microscopy (HRTEM) analysis was conducted on an individual PMA<sub>2</sub>PbCl<sub>4</sub> MMB to determine its monocrystalline property and growth direction. Figure 1c shows two lattice spacings of 0.40 and 0.38 nm, corresponding to the (020) and (002) planes of the 2D PMA<sub>2</sub>PbCl<sub>4</sub> MMB, respectively. Moreover, the corresponding SAED image via fast Fourier transform (FFT) in the inset of Figure 1c can be indexed to the [100] zone axis. Therefore, the 2D PMA<sub>2</sub>PbCl<sub>4</sub> MMBs grow along [001] direction, and they belong to the orthorhombic crystal structure, which is consistent with early reported PMA<sub>2</sub>PbCl<sub>4</sub> bulk single crystals.<sup>32</sup> Figure 1d shows the photoluminescence (PL) spectrum (blue) and optical absorption spectrum (red), with a PL peak locating at 350 nm and an absorption edge at 340 nm, corresponding to a bandgap of 3.63 eV (inset of Figure 1d), indicating that PMA<sub>2</sub>PbCl<sub>4</sub> perovskite is a wide bandgap semiconductor. A bandgap of 3.63 eV is in agreement with the reported value 3.65 eV of PMA<sub>2</sub>PbCl<sub>4</sub> single crystal.<sup>32</sup>

Figure 1e shows the X-ray diffraction (XRD) patterns of PMA<sub>2</sub>PbCl<sub>4</sub> MMBs containing a series of sharp and well-defined periodically distributed diffraction peaks (*h*00) (*h* = 2, 4, 6...), demonstrating that the PMA<sub>2</sub>PbCl<sub>4</sub> MMBs have good crystallinity with a highly preferred orientation, which is consistent with the TEM results.<sup>32</sup> The energy-dispersive X-ray spectroscopy (EDS) mapping analysis was further conducted to show the distribution of elements based on the sample obtained via the focused ion beam (FIB) method (SI Figure S2), from which one can see that the C, Pb, and Cl elements are uniformly distributed within the MMB across the entire imaging area.

Figure 2a shows the time-resolved PL (TRPL) curve obtained using a 275 nm excitation wavelength, which demonstrates a biexponential decay feature with a fast photocarrier lifetime ( $\tau_1 = 1.25$  ns) and a slow component lifetime ( $\tau_2 = 2.56$  ns), which are related to the surface recombination and bulk recombination, respectively. To determine the energy band structure of PMA<sub>2</sub>PbCl<sub>4</sub> MMBs, the ultraviolet photoelectron spectroscopy (UPS) spectrum was measured, and the result is shown in Figure 2b. The Fermi

level of  $\text{PMA}_2\text{PbCl}_4$  MMBs is located at  $-5.10$  eV, and the valence band edge at  $-6.69$  eV, relative to the vacuum level. Therefore, the conduction band is located at  $-3.06$  eV since the optical band gap is  $3.63$  eV. The inset shows the corresponding energy band diagram. In addition, X-ray photoelectron spectroscopy (XPS) spectra were taken for attaining the chemical state of Pb and Cl in the  $\text{PMA}_2\text{PbCl}_4$  MMB (Figure 2c). The peaks of Pb 4f ( $138.40$  and  $143.25$  eV) and Cl 2p ( $196.40$  and  $198$  eV) can be attributed to the Pb–Cl bonds in  $\text{PMA}_2\text{PbCl}_4$  MMB. Polarization-electric field ( $P$ – $E$ ) hysteresis loop of  $\text{PMA}_2\text{PbCl}_4$  MMB confirms the presence of the ferroelectricity of  $\text{PMA}_2\text{PbCl}_4$  MMB (Figure 2d). The space charge limited current method (SCLC) was then used to investigate the trap densities of  $\text{PMA}_2\text{PbCl}_4$  MMBs. Therefore, both hole-only devices (Au/ $\text{PMA}_2\text{PbCl}_4$ /Au) and electron-only devices (Ag/PC61BM/ $\text{PMA}_2\text{PbCl}_4$ /PC61BM/Ag) were fabricated (Figure 2e,f). By measuring the dark current–voltage ( $I$ – $V$ ) curves for the two devices, trap densities can be calculated with the following equation:

$$n_{\text{trap}} = \frac{2\varepsilon_0\varepsilon_r V_{\text{TFL}}}{eL^2}$$

where  $\varepsilon_0$  is the vacuum permittivity,  $\varepsilon_r$  is the relative dielectric constant,  $V_{\text{TFL}}$  is the trap-filled limit voltage,  $e$  is the electron charge, and  $L$  is the distance between two electrodes. Here,  $\varepsilon_r$  is obtained from the reported result.<sup>44</sup> Therefore, the hole-trap density and electron-trap density were calculated as  $6.52 \times 10^9$  and  $5.71 \times 10^{10} \text{ cm}^{-3}$ , respectively. Therefore,  $\text{PMA}_2\text{PbCl}_4$  MMBs with a relative wide bandgap, good ferroelectricity, low defect density, and definite orientation are ideal platforms for the fabrication of self-powered UV PDs.

Then the 2D  $\text{PMA}_2\text{PbCl}_4$  MMBs were designed and fabricated into an M–S–M structure with two parallel electrodes lying on two ends of the MMBs. Here, two kinds of the metal electrodes, Au (100 nm Au layer) with high work function (5.1 eV) and Bi (Bi 20 nm/Ag 150 nm) with low work function (4.22 eV), are used to form the M–S–M structure. SI Figure S3a,b show the photoresponse spectra of the Ag/Bi/ $\text{PMA}_2\text{PbCl}_4$  MMB/Bi/Ag PD and Au/ $\text{PMA}_2\text{PbCl}_4$  MMB/Au PD illuminated using monochromatic light with a wavelength ranging from 240 to 800 nm under the same power density ( $31.8 \mu\text{W}/\text{cm}^2$ ) at zero bias, respectively. The corresponding  $I$ – $t$  curves of the two types of PDs at typical wavelength (280, 320, 400, 520, 680, and 800 nm) are exhibited in SI Figure S3c,d. Both two types of PDs show the highest response at 320 nm, which is consistent with their optical absorption cutoff edge of 2D  $\text{PMA}_2\text{PbCl}_4$  MMB. Figure 3a illustrates the device structure, and a 320 nm laser is used as the major light source to determine the PDs' performances. The  $I$ – $V$  characteristics of the PDs with Bi/Ag electrode and Au electrode under 320 nm laser illumination with different power densities are shown in Figure 3b and SI Figure S4a, respectively. For both types of PDs, when laser power density rises from 0 to  $31.8 \mu\text{W}/\text{cm}^2$ , the current gradually increases, with a rather small increment even at 6 V. The asymmetry and nonlinear shapes of the curves demonstrate the formation of Schottky contact. And the Schottky barrier height ( $\Phi_b$ ) of the Ag/Bi/ $\text{PMA}_2\text{PbCl}_4$  MMB/Bi/Ag PD under dark condition is estimated to be 1.42 eV. Figure 3c schematically illustrates the working mechanism of the PDs. Under the dark conditions, the spontaneous polarization within the ferroelectric MMB along the  $c$  axis generates opposite polarization charges at two Schottky contacts. Therefore, free charges locate in the metal electrode

to guarantee electric neutrality. When the laser is turned on, on the one hand, the photoinduced electron and hole pairs will be generated and separated by the built-in ferroelectric field, forming a stable photocurrent. On the other hand, under light illumination, the surface temperature of the PDs increases, and the random oscillation state of electric dipoles within the MMB is disturbed, resulting in the decreased spontaneous polarization and less bound charges.<sup>45</sup> Therefore, the free charges located at the interfaces will flow to the contrary electrode, generating the positive output pyroelectric current. When laser continuously illuminates on the PDs, the temperature no longer changes, the pyroelectric current will vanish, leaving only a stable photocurrent. When the laser is turned off, the surface temperature of the PDs decreases, resulting in the increased spontaneous polarization and more bound charges, generating reversed pyroelectric current. The light-induced polarization charge can effectively modulate the transport of the charge carriers at the interface, which is the basic rule of the ferro-pyro-phototronic effect.

Furthermore, the  $I$ – $t$  curves of the Ag/Bi/ $\text{PMA}_2\text{PbCl}_4$  MMB/Bi/Ag PD under 320 nm laser illumination in different test conditions were systematically measured and analyzed. Figure 3d shows the zero-bias time-dependent on/off current of the self-powered PD (Bi/Ag electrode, 320 nm,  $31.8 \mu\text{W}/\text{cm}^2$ , 0.2 Hz of chopping frequency), from which one can see six cycles of stable and fast photoresponse. To confirm that the peak currents are caused by the pyroelectric effect, the  $I$ – $t$  curves of the PD with Bi/Ag electrode under dark condition by periodically rising the temperature are measured (SI Figure S5). From SI Figure S5, we can see that a positive current peak is observed as the temperature increases from 298 to 298.2 K ( $\Delta T = 0.2$  K). When the temperature decreases from 298.2 to 298 K, a negative current signal is obtained. Similarly, positive current peaks are observed when the temperature increase from 298 to 298.4 K ( $\Delta T = 0.4$  K) or 298.6 K ( $\Delta T = 0.6$  K) and the corresponding negative peaks are obtained by decreasing the temperature from 298.4 or 298.6 to 298 K. Additionally,  $I$ – $t$  characteristics of the  $\text{PMA}_2\text{PbCl}_4$  MMB PD with Bi/Ag electrode at forward connection and reversed connection with the testing system under 320 nm ( $31.8 \mu\text{W}/\text{cm}^2$ ) under zero bias at 0.2 Hz are demonstrated in SI Figure S6. The positive current signals are observed under forward connection while the opposite signs are obtained under reversed connection. This further proves the pyroelectric signal is induced by laser stimuli. When chopping frequency is low, there are only two sharp current peaks, while the stable photocurrent is not obvious. By further increasing chopping frequency, we found that pyroelectric currents and photocurrents highly depend on the chopping frequency.<sup>46</sup> SI Figure S7 shows the normalized  $I$ – $t$  curves of PD under 320 nm laser illumination with the same light power density and different chopping frequencies. Here, the positive pyroelectric current measured under 2 Hz is used as current reference value, and other currents are normalized. With the frequency increasing from 2 to 200 Hz, both pyroelectric currents and photocurrents are enhanced obviously, with a nearly two times enhancement for positive currents, due to that the pyroelectric currents are proportional to temperature alteration rate  $dT/dt$ .<sup>36</sup> However, further increasing the chopping frequency to 600 Hz will decrease pyroelectric currents, while the photocurrent still increases. When the frequency exceeds 1000 Hz, pyroelectric currents disappear. The mechanism of increased photocurrent induced by chopping frequency will be

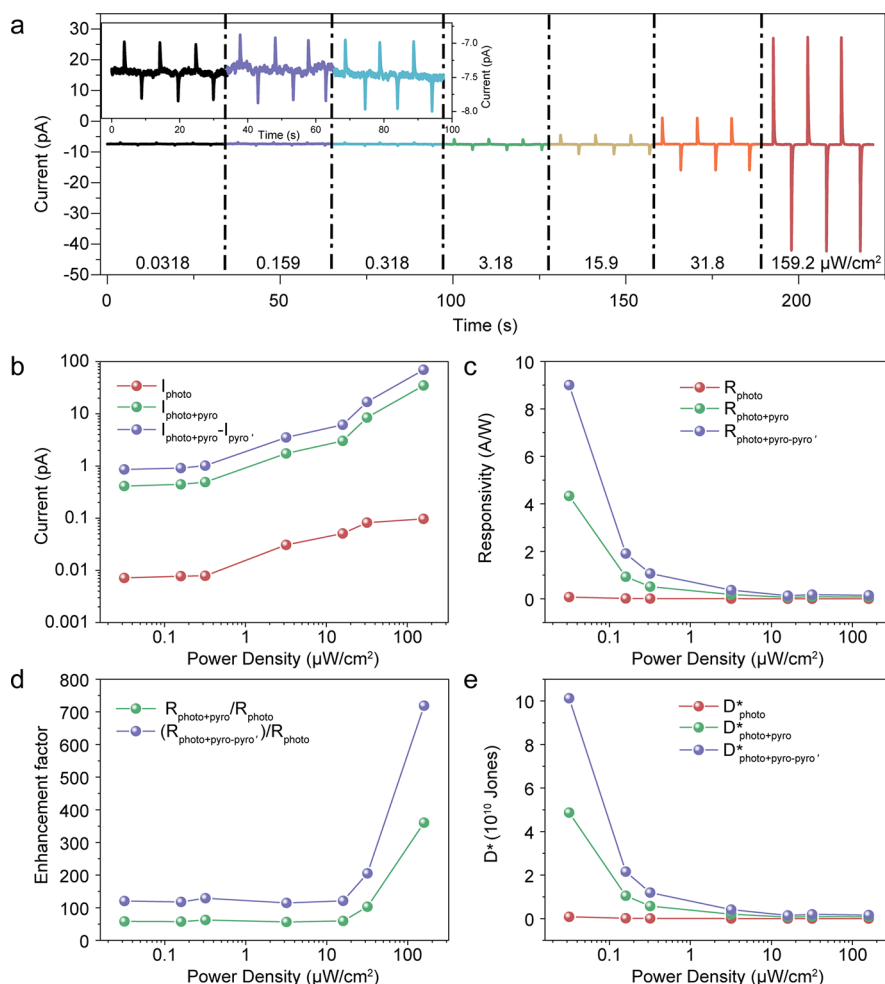


**Figure 4.** UV photodetection capability of the self-powered Ag/Bi/2D PMA<sub>2</sub>PbCl<sub>4</sub> MMB/Bi/Ag PD under 320 nm laser illumination at zero bias. (a)  $I-t$  characteristics of the PD with different power densities from 0.0318 to 159  $\mu\text{W}/\text{cm}^2$ . The inset is the corresponding enlarged  $I-t$  curves from 0.0318 to 0.318  $\mu\text{W}/\text{cm}^2$ . (b)  $I_{\text{photo}}$ ,  $I_{\text{pyro+photo}}$ , and  $I_{\text{pyro+photo}} - I_{\text{pyro'}}$ , (c) corresponding  $R_{\text{photo}}$ ,  $R_{\text{pyro+photo}}$ , and  $R_{\text{pyro+photo-pyro'}}$ , (d) corresponding enhancement factor ( $R_{\text{pyro+photo}}/R_{\text{photo}}$  and  $R_{\text{pyro+photo-pyro'}}/R_{\text{photo}}$ ), and (e) corresponding  $D^*_{\text{photo}}$ ,  $D^*_{\text{pyro+photo}}$ , and  $D^*_{\text{pyro+photo-pyro'}}$  of the self-powered PD as a function of power density.

discussed later. Furthermore, we calculated and counted the response and recovery times of the PD with Bi/Ag electrode at different chopping frequencies (SI Figure S8). When the chopping frequency is 60 Hz, the PD with Bi/Ag electrode possesses the fastest response and recovery speeds. Figure 3e shows the obvious four-stage photoresponse behaviors of the PD under 320 nm laser illuminations with 60 Hz frequency, with a rise time of 162  $\mu\text{s}$  and a fall time of 226  $\mu\text{s}$ , indicating fast rise and fall speed. In addition, the four-stage photo response behavior shows the  $I_{\text{pyro+photo}}$  is an instantaneous output current and much larger than the  $I_{\text{photo}}$ , which is conducive to realizing fast, and high-sensitive photodetecting. This four-stage photoresponse behavior is consistent with the mechanism in Figure 3c. Figure 3f shows the plot of the frequency responses of the PD, with a  $-3$  dB cutoff frequency up to 2600 Hz. The photoresponse of Au/PMA<sub>2</sub>PbCl<sub>4</sub> MMB/Au PD demonstrates a similar trend at different chopping frequencies (SI Figures S9 and S10). The chopping frequencies of the inflection points correspond to 200, 600, and 900 Hz. As shown in SI Figure S4b,c, the rise/fall time at 60 Hz and  $-3$  dB cutoff frequency are 176/260  $\mu\text{s}$  and 2777 Hz, respectively. These results are close to the performance of the PD with Bi/Ag electrode. The enhancement of photocurrent plateau would

be explained by the modulation of ferro-pyro-phototronic effect on the energy band diagrams, as described in Figure 3g. The structure of the fabricated PDs can be considered as a sandwich structure of PMA<sub>2</sub>PbCl<sub>4</sub> layer sandwiched between the left and right Schottky barrier interfaces. The negative polarized charges are obtained from the left interface, while the positive polarized charges are obtained from the right interface, leading to the upward and downward bending of the energy band, respectively. When 320 nm laser is turned on, the device's temperature will increase, resulting in the reduced negative and positive polarized charges both at two interfaces. Therefore, the Schottky barrier height is reduced. Higher chopping frequency will reduce the Schottky barriers height, which is favorable to the photogenerated carriers' flow, resulting in larger photocurrent. When the 320 nm laser is turned off, the photocurrent disappears, and the device's temperature will decrease, resulting in the enhanced negative and positive polarized charges and the elevated Schottky barriers height. This can further be confirmed by calculating Schottky barrier height at different temperatures (SI Figure S11). It is obvious that the barrier height decreases with the increase of temperature, which well confirms the above view.

**Table 1. Comparative Performance Parameters of Previously Reported Self-Powered UV PDs and the Present PMA<sub>2</sub>PbCl<sub>4</sub> MMB-based PD**

active materials	wavelength (nm)	responsivity (A/W)	detectivity (Jones)	rise time (s)	decay time (s)	ref
InSe/Au	365	0.369	$2.56 \times 10^{11}$	0.068	0.075	47
CdS/Si	325	$5.9 \times 10^{-3}$	$1.0 \times 10^{12}$	$\sim 2.5 \times 10^{-4}$	$\sim 2.7 \times 10^{-4}$	36
GaN/Sn:Ga <sub>2</sub> O <sub>3</sub>	254	3.05	$1.69 \times 10^{13}$	0.018		6
ZnO Nanofiber	360	$1.28 \times 10^{-5}$		3.9	4.71	4
ZnO nanorod arrays	UV	$2.45 \times 10^{-5}$	$4.17 \times 10^9$	4.78	0.33	48
Multilayer $\gamma$ -InSe	400	0.824	$8.7 \times 10^{11}$	$2.03 \times 10^{-5}$	$1.08 \times 10^{-5}$	49
BaTiO <sub>3</sub>	405	$7.5 \times 10^{-6}$	$\sim 9 \times 10^9$	0.88	1.06	39
ZnS SSNWs	265	0.0194	$9.6 \times 10^{11}$	0.25	0.2	50
bis(dithiolene) iron(II) coordination nanosheet	365	$6.57 \times 10^{-3}$	$3.13 \times 10^{11}$	$\sim 0.03$	$\sim 0.03$	51
ZnO NWs/SnS	365	$1.55 \times 10^{-4}$		49.1	51.8	52
(BPA) <sub>2</sub> PbBr <sub>4</sub>	377	$\sim 10^{-4}$	$\sim 10^7$	$2.7 \times 10^{-5}$	$3 \times 10^{-5}$	30
NiO/PLZT heterojunction	350	$6.3 \times 10^{-4}$	$1.29 \times 10^{10}$	0.34	0.36	53
(PMA) <sub>2</sub> PbCl <sub>4</sub> MMB	320	9	$1.01 \times 10^{11}$	$1.62 \times 10^{-4}$	$2.26 \times 10^{-4}$	this work

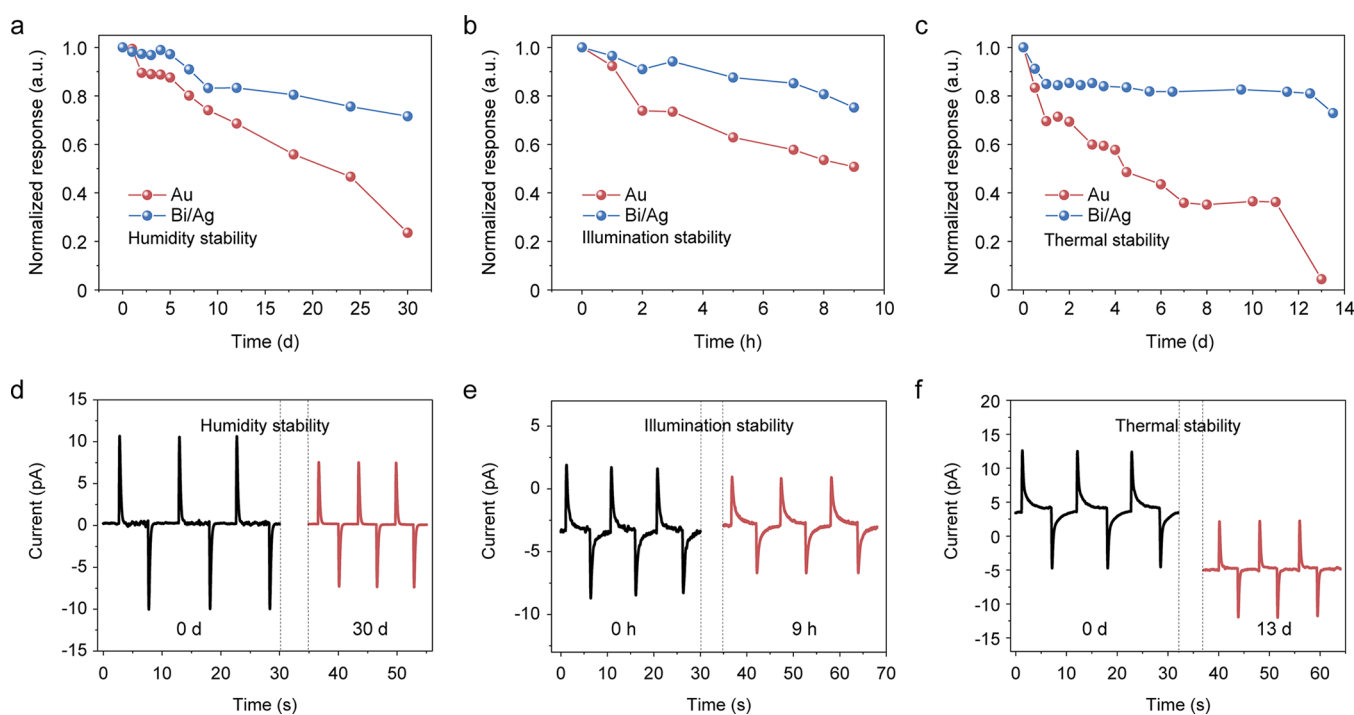


**Figure 5.** Stability of the 2D PMA<sub>2</sub>PbCl<sub>4</sub> MMB-based self-powered PDs (Au electrode and Bi/Ag electrode). (a) Comparison of humidity stability of two types of unencapsulated devices stored in the  $70 \pm 10\%$  humidity at RT. (d) The corresponding  $I-t$  characteristics of the PD with Bi/Ag electrode to the 320 nm laser illumination ( $31.8 \mu\text{W}/\text{cm}^2$ ) after 0 and 30 days. (b) Illumination stability of two types of unencapsulated PDs aged under continuous 320 nm laser illumination ( $159 \mu\text{W}/\text{cm}^2$ ) in  $70 \pm 10\%$  humidity conditions at RT. (e) The corresponding  $I-t$  characteristics of the device with Bi/Ag electrode to the 320 nm laser illumination ( $31.8 \mu\text{W}/\text{cm}^2$ ) after 0 and 9 h. (c) Thermal stability of two types of unencapsulated devices aged under continuous heating at  $85^\circ\text{C}$  in a N<sub>2</sub>-filled glovebox. (f) The corresponding  $I-t$  characteristics of the device with Bi/Ag electrode to the 320 nm laser illumination ( $31.8 \mu\text{W}/\text{cm}^2$ ) after 0 and 13 days.

The photoresponses of the self-powered PD based on 2D PMA<sub>2</sub>PbCl<sub>4</sub> MMB under 320 nm laser illumination at zero bias are systematically measured and evaluated in Figure 4 (Bi/Ag electrode) and SI Figure S12 (Au electrode). From Figure 4a and SI Figure 12a, one can see that the  $I-t$  curves with power density ranging from  $3.18$  to  $159 \mu\text{W}/\text{cm}^2$  at zero bias show obvious and stable four-stage photoresponse behaviors. Due to the higher current at  $159 \mu\text{W}/\text{cm}^2$ , the photoresponse currents from  $0.0318$  to  $0.318 \mu\text{W}/\text{cm}^2$  seem insignificant. When the  $I-t$  curves from  $0.0318$  to  $0.318 \mu\text{W}/\text{cm}^2$  were enlarged, the four-stage photoresponse behaviors of these curves are also obvious (the inset of Figure 4a and SI Figure S12a). Besides, the pyroelectric currents increase with the

increased power density due to that the higher incident power density will result in faster temperature-change rate ( $dT/dt$ ). However, compared with the pyroelectric currents, the photocurrents are too small to be observed. Furthermore, the relative peak-to-peak output current ( $I_{\text{pyro+photo}} - I_{\text{pyro}}$ ), the  $I_{\text{pyro+photo}}$  and  $I_{\text{photo}}$  are extracted from Figure 4a and SI Figure S12a and drawn as a function of power density in Figure 4b and SI Figure S12b. All the three output currents increase with the increase of power density. Moreover, the pyroelectric currents ( $I_{\text{pyro+photo}} - I_{\text{pyro}}$ ) and the  $I_{\text{pyro+photo}}$  are much higher than the  $I_{\text{photo}}$ . The responsivity  $R$ , and specific detectivity  $D^*$  are calculated as following equations:

$$R = \frac{(I_{\text{photo}} - I_{\text{d}})/S}{P}$$

and

$$D^* = \frac{R}{\sqrt{2eI_{\text{d}}/S}}$$

where  $I_{\text{photo}}$  is the photocurrent,  $I_{\text{d}}$  is the dark current,  $S$  is the active area of the PD, and  $P$  is the light power density illuminated onto the device. Here,  $I_{\text{d}}$  of PD with Bi/Ag electrode is about  $-7.52 \times 10^{-12}$  A,  $I_{\text{d}}$  of PD with Au electrode is about  $-1.23 \times 10^{-11}$  A (SI Figure S13), and  $S$  is  $3 \times 10^{-10}$  m<sup>2</sup> (SI Figure S14). The corresponding responsivities are calculated and plotted in Figure 4c and SI Figure S12c. The three responsivities show a decreasing tendency with the rise of the power density, and the  $R_{\text{pyro+photo-pyro}}$  and  $R_{\text{pyro+photo}}$  are always higher than the  $R_{\text{photo}}$ . When the power density is  $0.0318 \mu\text{W}/\text{cm}^2$ , the  $R_{\text{pyro+photo-pyro}}$ ,  $R_{\text{pyro+photo}}$ , and  $R_{\text{photo}}$  reach the maximum value. For the PD with Bi/Ag electrode, the maximum values of  $R_{\text{pyro+photo-pyro}}$ ,  $R_{\text{pyro+photo}}$ , and  $R_{\text{photo}}$  are 9, 4.33, and 0.07 A/W, respectively. For the PD with Au electrode, the maximum values of  $R_{\text{pyro+photo-pyro}}$ ,  $R_{\text{pyro+photo}}$ , and  $R_{\text{photo}}$  are 5.27, 2.24, and 0.02 A/W, respectively. The photodetection performances of the previously reported self-powered UV PDs and the present PMA<sub>2</sub>PbCl<sub>4</sub> MMB-based PD are listed in Table 1, from which one can see that our UV PDs demonstrate comparable detectivity, response/recovery time, and the highest photoresponsivity. As shown in Figure 4d, compared with the  $R_{\text{photo}}$ , the increase multiples of  $R_{\text{pyro+photo-pyro}}$  and  $R_{\text{pyro+photo}}$  are as high as 128.6 times and 61.9 times, respectively, attributing to the introduction of the ferro-pyro-phototronic effect. The corresponding  $D^*_{\text{photo}}$ ,  $D^*_{\text{pyro+photo}}$ , and  $D^*_{\text{pyro+photo-pyro}}$  as a function of the power density were shown in Figure 4e. Similarly, the maximum value of  $D^*$  is  $1.01 \times 10^{11}$  Jones for  $D^*_{\text{pyro+photo-pyro}}$ . The maximum value of  $D^*$  the self-powered PDs with Au electrode is about  $4.5 \times 10^{10}$  Jones (SI Figure S12e). Furthermore, we measured 15 PDs with Au electrode and 15 PDs with Bi/Ag electrode to evaluate the PDs' performances (SI Figure S15). SI Figure S15a shows averaged lowest detectable power density by each of these PDs with two types of electrodes. The PDs with Bi/Ag electrode could detect lower power density than the PDs with Au electrode, and the detectable power density is as low as  $0.0318 \mu\text{W}/\text{cm}^2$ , which is consistent with above results (Figure 4a). While the maximum responsivity of the PDs with Au electrode is close to that of the PDs with Bi/Ag electrode (SI Figure S15b). Furthermore, the  $I-t$  curves of the PDs with Bi/Ag electrode at different forward and reversed bias under 320 nm laser illumination ( $31.8 \mu\text{W}/\text{cm}^2$ ) at 0.2 Hz are measured to evaluate the bias voltage effect on the pyro-phototronic effect (SI Figure S16). As the forward bias voltage increases from 0.5 to 2.0 V, the four-stage photoresponse behavior gradually decreases (0.5–1.5 V) until disappears at 2.0 V, which should be attributed to joule heat caused by external bias impairing pyro-phototronic effect. Similarly, when the reversed bias voltage reaches  $-2.0$  V, the pyroelectric currents disappear.

It is known to all that stability of the perovskite-based devices is the critical factor to estimate the capability for practical application. We systematically compared the stability of two types of unencapsulated self-powered 2D PMA<sub>2</sub>PbCl<sub>4</sub> MMB-based PDs under high humidity, intense laser illumination, and thermal environment in Figure 5 (Bi/Ag

electrode) and SI Figure S17 (Au electrode). The normalized responses of typical PDs as a function of the aging time are shown in Figure 5a–c. Figure 5a presents the stability of two types of unencapsulated devices stored in  $70 \pm 10\%$  humidity conditions at room temperature (RT). The PDs with Bi/Ag electrode possess higher moisture stability than the PDs with Au electrode. The corresponding  $I-t$  characteristics of two types of PDs under 320 nm laser illumination ( $31.8 \mu\text{W}/\text{cm}^2$ ) after just fabricated and after 30 days are shown in Figure 5d (Bi/Ag electrode) and SI Figure S17a (Au electrode). After 30 days, the PDs with Bi/Ag electrode maintained approximately 71.6% of its initial response, while the PDs with Au electrode maintained only about 23.5% of its initial response. That is due to the Bi interlayer behaving as a robust diffusion barrier which both protects the perovskites from moisture and hinders the permeation of atoms in electrodes into perovskites.<sup>43</sup> Similarly, the Bi interlayer also had a positive effect on light soaking and thermal aging conditions. The PDs with the Bi interlayer retained approximately 75.2% after continuous 320 nm laser illumination ( $159 \mu\text{W}/\text{cm}^2$ ) in ambient air ( $70 \pm 10\%$  RH) at RT for 9 h (Figure 5b,e), and 72.9% of their initial responses after continuous heating at 85 °C in a N<sub>2</sub>-filled glovebox for 13 days (Figure 5c and f). By contrast, the PDs with Au electrode maintained only 50.7% and 4.4% of their initial responses after the corresponding aging tests (Figure 5b,c, SI Figure S17b,c). Therefore, the PDs with low-cost Bi interlayer electrode show much higher stability than the PDs with commonly used Au electrode under different conditions. In addition, the long-term stability of two types of unencapsulated devices stored in the open environment ( $25 \pm 5\%$  humidity at RT) is shown in SI Figure S18a. After 91 days, the PD with Bi/Ag electrode and the PD with Au electrode maintained about 85.1% and 60.7% of their initial responses (SI Figure S18b,c), respectively. These results prove self-powered 2D PMA<sub>2</sub>PbCl<sub>4</sub> MMB-based PD with Bi/Ag electrode has outstanding stability.

## CONCLUSION

In summary, we have successfully built the high-performance and stable self-powered UV PDs based on 2D ferroelectric PMA<sub>2</sub>PbCl<sub>4</sub> MMB with the aid of ferro-pyro-phototronic effect. 2D ferroelectric PMA<sub>2</sub>PbCl<sub>4</sub> MMBs with good orientation and high quality were grown by a space-confined assisted antisolvent growth method. By introducing the light-induced ferro-pyro-phototronic effect to modulate the optoelectronic processes, the self-powered UV PDs based on 2D ferroelectric PMA<sub>2</sub>PbCl<sub>4</sub> MMB under zero bias show a fast response/recovery speed of 162/226 μs, and high responsivity of 9 A/W, which is the highest value compared with other previously reported self-powered UV PDs so far. Moreover, the PDs with inert Bi interlayer electrode display excellent humidity, light, and thermal stability than the devices with Au electrode. Especially, the unencapsulated PDs with Bi interlayer electrode retains 71.6% of initial response after being stored in  $70 \pm 10\%$  humidity conditions at RT for 30 days. Our work will offer an effective way of coupling ferro-pyro-phototronic effect on prominent optoelectronic devices made from ferroelectric perovskites and develop high-performance and self-powered UV PDs.

## METHODS

**Materials.** *N,N*-Dimethylformamide (DMF, 99.9%), and anisole (99.9%) were purchased from Shanghai Macklin Biochemical Co., Ltd. Lead chloride (PbCl<sub>2</sub>, 99.99%) and benzylamine hydrochloride

(PMAcI, 99.99%) were purchased from Xian Polymer light Technology Corp. All the chemicals were used as received without further purification.

#### Growth of PMA<sub>2</sub>PbCl<sub>4</sub> Monocrystalline Microbelts (MMBs).

The crystallization procedure of the MMBs is schematically drawn in Figure 1a. Briefly, PMAcI, and PbCl<sub>2</sub> (2:1 molar ratio) were dissolved in DMF at room temperature under magnetic stirring for 12 h to generate the PMA<sub>2</sub>PbCl<sub>4</sub> precursor solution (0.05–0.1 M). The solution was then filtered using 0.22 μm PTFE filters before crystal growth. A Si/SiO<sub>2</sub> wafer was cut into 1 cm × 1 cm slices, and the slices were washed with deionized acetone, absolute ethyl alcohol, and water successively, then been dried with purged N<sub>2</sub> flow, followed by 10 min O<sub>2</sub> plasma treatments. For the growth of the PMA<sub>2</sub>PbCl<sub>4</sub> MMBs, a small amount of precursor solution (2–3 μL) was dropped onto the Si/SiO<sub>2</sub> slice. Then another slice was placed onto the precursor solution drop, and a large pressure (~150 kPa) was applied onto the slices using an adjustable clamp. Then the apparatus was transferred into a sealed desiccator containing 500 mL of anisole solvent placed inside a 40 °C oven. The MMBs would gradually grow up with anisole vapor diffusing into the solution. After 48 hours growth, the DMF solvent will totally volatilize, and the MMBs will be obtained after the separation of the two slices.

**Fabrication of the PMA<sub>2</sub>PbCl<sub>4</sub> Planar PDs.** Planar PDs were fabricated by depositing interdigital electrodes (Au electrode: 100 nm thickness; Bi/Ag electrode: 20/150 nm thickness.) via vacuum evaporation method onto the PMA<sub>2</sub>PbCl<sub>4</sub> MMBs using the metal mask. The gap between two electrodes is about 20 μm.

**Characterization.** XRD patterns were collected using a Bruker D8 Advance X-ray diffractometer equipped with a Cu tube ( $\lambda = 1.5406$  Å) operated at 40 kV and 20 mA. UV–vis absorbance spectrum was measured using a Hitachi U4100 UV–vis-NIR spectrophotometer. UPS was performed on a photoelectron spectrometer (Thermo, ESCALAB 250 Xi) to analyze the working function of the PMA<sub>2</sub>PbCl<sub>4</sub> MMBs. Steady-state and time-resolved PL measurements were taken using an FLS920 (Edinburgh Instruments) fluorescence spectrometer with 275 nm excitation wavelength. The thickness of the PMA<sub>2</sub>PbCl<sub>4</sub> MMBs was measured using a stylus profiler (Bruker, DektakXT). The morphology and structure characterizations of the PMA<sub>2</sub>PbCl<sub>4</sub> MMBs were performed using SEM (Nova Nano-SEM450) and HRTEM (JEOL, JEM-ARM200F).

**SCLC Measurements.** The electron-only, and hole-only devices were fabricated to determine the trap-state density using the SCLC method. The PMA<sub>2</sub>PbCl<sub>4</sub> MMBs in around 300 nm thickness on SiO<sub>2</sub> (500 nm)/Si substrate were patterned with two electrodes. The structures are Au/PMA<sub>2</sub>PbCl<sub>4</sub>/Au for hole-only devices and Ag/PC61BM/PMA<sub>2</sub>PbCl<sub>4</sub>/PC61BM/Ag for electron-only devices. The dark *I*–*V* curves were measured using the Keithley 4200 source meter, and then cutoff voltages deduced from the curves were used to calculate the trap-state density.

**Photodetection Performance Measurements.** The *I*–*V* characteristics were measured using the Keithley 4200 semiconductor characterization system under dark and illumination conditions. The *I*–*t* curves were recorded by coupling a Stanford SRS current preamplifier (SR570) and a Stanford SRS function generator (DS345). To measure the response and recovery speed, the temporal response of the device was measured using a Mixed Domain Oscilloscope (Tektronix, MDO3104). A chopper (SR540, Stanford) was used to generate pulsed laser beams. The 320 nm laser (Changchun New Industries Optoelectronics Technology Co., Ltd.) was used as the major laser source. For wavelength-dependent photocurrent measurement, the monochromatic lights were provided by a mercury lamp equipped with a monochromator (NBeT, omno3001000). The light power intensity was measured using an optical power meter (PM100D) and calibrated with a silicon PD.

**Stability Test.** The humidity stability of the unencapsulated PDs was performed by storing devices in 70 ± 10% humidity conditions at RT. Light soaking stability of the unencapsulated PDs was carried out under continuous 320 nm laser illumination (159 μW/cm<sup>2</sup>) in ambient air at RT. The thermal stability of the unencapsulated PDs was performed by continuous heating of the devices at 85 °C in a N<sub>2</sub>-

filled glovebox. All PDs were tested under 320 nm laser illumination (31.8 μW/cm<sup>2</sup>) for *I*–*t* characterization at regular intervals. The RH in the laboratory was within 70 ± 10% during the entire aging test.

## ASSOCIATED CONTENT

### Supporting Information

The Supporting Information is available free of charge at <https://pubs.acs.org/doi/10.1021/acsnano.1c09119>.

SEM image, photograph, height distribution, and EDS analysis of 2D ferroelectric PMA<sub>2</sub>PbCl<sub>4</sub> MMB; photo-response spectra, *I*–*V* characteristics, *I*–*t* characteristics, dark currents, active area, and stability of devices (DOCX)

## AUTHOR INFORMATION

### Corresponding Authors

**Shufang Wang** – Hebei Key Laboratory of Optic-Electronic Information and Materials, National & Local Joint Engineering Laboratory of New Energy Photoelectric Devices, College of Physics Science and Technology, Hebei University, Baoding 071002, P. R. China; Email: [sfwang@hbu.edu.cn](mailto:sfwang@hbu.edu.cn)

**Caofeng Pan** – CAS Center for Excellence in Nanoscience, Beijing Institute of Nanoenergy and Nanosystems, Chinese Academy of Sciences, Beijing 100083, P. R. China; [orcid.org/0000-0001-6327-9692](https://orcid.org/0000-0001-6327-9692); Email: [cfpan@binn.cas.cn](mailto:cfpan@binn.cas.cn)

**Zheng Yang** – Hebei Key Laboratory of Optic-Electronic Information and Materials, National & Local Joint Engineering Laboratory of New Energy Photoelectric Devices, College of Physics Science and Technology, Hebei University, Baoding 071002, P. R. China; CAS Center for Excellence in Nanoscience, Beijing Institute of Nanoenergy and Nanosystems, Chinese Academy of Sciences, Beijing 100083, P. R. China; [orcid.org/0000-0001-7172-4717](https://orcid.org/0000-0001-7172-4717); Email: [yangzheng06@hbu.edu.cn](mailto:yangzheng06@hbu.edu.cn)

### Authors

**Linjuan Guo** – Hebei Key Laboratory of Optic-Electronic Information and Materials, National & Local Joint Engineering Laboratory of New Energy Photoelectric Devices, College of Physics Science and Technology, Hebei University, Baoding 071002, P. R. China

**Xiu Liu** – Hebei Key Laboratory of Optic-Electronic Information and Materials, National & Local Joint Engineering Laboratory of New Energy Photoelectric Devices, College of Physics Science and Technology, Hebei University, Baoding 071002, P. R. China

**Linjie Gao** – Hebei Key Laboratory of Optic-Electronic Information and Materials, National & Local Joint Engineering Laboratory of New Energy Photoelectric Devices, College of Physics Science and Technology, Hebei University, Baoding 071002, P. R. China

**Xinzhan Wang** – Hebei Key Laboratory of Optic-Electronic Information and Materials, National & Local Joint Engineering Laboratory of New Energy Photoelectric Devices, College of Physics Science and Technology, Hebei University, Baoding 071002, P. R. China

**Lei Zhao** – Hebei Key Laboratory of Optic-Electronic Information and Materials, National & Local Joint Engineering Laboratory of New Energy Photoelectric Devices, College of Physics Science and Technology, Hebei University, Baoding 071002, P. R. China; [orcid.org/0000-0001-9226-2929](https://orcid.org/0000-0001-9226-2929)

Wei Zhang – Hebei Key Laboratory of Optic-Electronic Information and Materials, National & Local Joint Engineering Laboratory of New Energy Photoelectric Devices, College of Physics Science and Technology, Hebei University, Baoding 071002, P. R. China

Complete contact information is available at:  
<https://pubs.acs.org/10.1021/acsnano.1c09119>

### Author Contributions

L.G. and X.L. contributed equally to this work. Z.Y. conceived and supervised the project. L.G. and X.L. synthesized the perovskites, fabricated the devices, and measured the optoelectronic properties. X.W. contributed to the PL measurement. L.Z. and W.Z. contributed to the ferroelectric measurement. L.G. wrote the manuscript. Z.Y. modified it. S.W. and C.P. provided funding support and critical suggestions for this work. All the authors reviewed the manuscript.

### Notes

The authors declare no competing financial interest.

### ACKNOWLEDGMENTS

This work was supported by the National Natural Science Foundation of China (Grant Nos. 62005072, 62104057, 51972094, 52125205, U20A20166, 61805015, and 61804011), the Natural Science Foundation of Hebei Province (Grant Nos. E2020201025, E2021201016, and B2021201034), the Advanced Talents Incubation Program of the Hebei University (521000981287, 521000981351, and 521000981248), the Undergraduate Innovation and Entrepreneurship Training Program of the Hebei University (2021174 and 2021172), Natural Science Foundation of Beijing Municipality (Z180011), Shenzhen Science and Technology Program (Grant No. KQTD20170810105439418) and the Fundamental Research Funds for the Central Universities.

### REFERENCES

- (1) Li, S.; Zhang, Y.; Yang, W.; Liu, H.; Fang, X. 2D Perovskite  $\text{Sr}_2\text{Nb}_3\text{O}_{10}$  for High-Performance UV Photodetectors. *Adv. Mater.* **2020**, *32*, 1905443.
- (2) Zhang, Y.; Zhao, X.; Chen, J.; Li, S.; Yang, W.; Fang, X. Self-Polarized  $\text{BaTiO}_3$  for Greatly Enhanced Performance of ZnO UV Photodetector by Regulating the Distribution of Electron Concentration. *Adv. Funct. Mater.* **2020**, *30*, 1907650.
- (3) Zhao, R.; Ma, N.; Song, K.; Yang, Y. Boosting Photocurrent via Heating  $\text{BiFeO}_3$  Materials for Enhanced Self-Powered UV Photodetectors. *Adv. Funct. Mater.* **2020**, *30*, 1906232.
- (4) Ning, Y.; Zhang, Z.; Teng, F.; Fang, X. Novel Transparent and Self-Powered UV Photodetector Based on Crossed ZnO Nanofiber Array Homojunction. *Small* **2018**, *14*, 1703754.
- (5) Ouyang, W.; Teng, F.; Fang, X. High Performance  $\text{BiOCl}$  Nanosheets/ $\text{TiO}_2$  Nanotube Arrays Heterojunction UV Photodetector: The Influences of Self-Induced Inner Electric Fields in the  $\text{BiOCl}$  Nanosheets. *Adv. Funct. Mater.* **2018**, *28*, 1707178.
- (6) Guo, D.; Su, Y.; Shi, H.; Li, P.; Zhao, N.; Ye, J.; Wang, S.; Liu, A.; Chen, Z.; Li, C.; Tang, W. Self-Powered Ultraviolet Photodetector with Superhigh Photoresponsivity (3.05 A/W) Based on the  $\text{GaN}/\text{Sn:Ga}_2\text{O}_3$  pn Junction. *ACS Nano* **2018**, *12*, 12827–12835.
- (7) Xie, C.; Lu, X.; Tong, X.; Zhang, Z.; Liang, F.; Liang, L.; Luo, L.; Wu, Y. Recent Progress in Solar-Blind Deep-Ultraviolet Photodetectors Based on Inorganic Ultrawide Bandgap Semiconductors. *Adv. Funct. Mater.* **2019**, *29*, 1806006.
- (8) Dubey, A.; Mishra, R.; Hsieh, Y.; Cheng, C.; Wu, B.; Chen, L.; Gwo, S.; Yen, T. Aluminum Plasmonics Enriched Ultraviolet GaN

Photodetector with Ultrahigh Responsivity, Detectivity, and Broad Bandwidth. *Adv. Sci.* **2020**, *7*, 2002274.

(9) Song, W.; Chen, J.; Li, Z.; Fang, X. Self-Powered MXene/GaN van der Waals Heterojunction Ultraviolet Photodiodes with Superhigh Efficiency and Stable Current Outputs. *Adv. Mater.* **2021**, *33*, 2101059.

(10) Jeong, J.; Kim, M.; Seo, J.; Lu, H.; Ahlawat, P.; Mishra, A.; Yang, Y.; Hope, M. A.; Eickemeyer, F.; Kim, M.; Yoon, Y.; Choi, I.; Darwich, B.; Choi, S.; Jo, Y.; Lee, J.; Walker, B.; Zakeeruddin, S.; Emsley, L.; Rothlisberger, U.; et al. Pseudo-Halide Anion Engineering for alpha-FAPbI<sub>3</sub> Perovskite Solar Cells. *Nature* **2021**, *592*, 381–385.

(11) Hui, W.; Chao, L.; Lu, H.; Xia, F.; Wei, Q.; Su, Z.; Niu, T.; Tao, L.; Du, B.; Li, D.; Wang, Y.; Dong, H.; Zuo, S.; Li, B.; Shi, W.; Ran, X.; Li, P.; Zhang, H.; Wu, Z.; Ran, C.; et al. Stabilizing Black-Phase Formamidinium Perovskite Formation at Room Temperature and High Humidity. *Science* **2021**, *371*, 1359–1364.

(12) Sun, J.; Li, N.; Dong, L.; Niu, X.; Zhao, M.; Xu, Z.; Zhou, H.; Shan, C.; Pan, C. Interfacial-Engineering Enhanced Performance and Stability of ZnO Nanowire-Based Perovskite Solar Cells. *Nanotechnology* **2021**, *32*, 475204.

(13) Liu, Y.; Zhang, Y.; Zhu, X.; Feng, J.; Spanopoulos, I.; Ke, W.; He, Y.; Ren, X.; Yang, Z.; Xiao, F.; Zhao, K.; Kanatzidis, M.; Liu, S. F. Triple-Cation and Mixed-Halide Perovskite Single Crystal for High-Performance X-ray Imaging. *Adv. Mater.* **2021**, *33*, 2006010.

(14) Feng, J.; Gong, C.; Gao, H.; Wen, W.; Gong, Y.; Jiang, X.; Zhang, B.; Wu, Y.; Wu, Y.; Fu, H.; Jiang, L.; Zhang, X. Single-Crystalline Layered Metal-Halide Perovskite Nanowires for Ultra-sensitive Photodetectors. *Nat. Electron.* **2018**, *1*, 404–410.

(15) Wu, W.; Wang, X.; Han, X.; Yang, Z.; Gao, G.; Zhang, Y.; Hu, J.; Tan, Y.; Pan, A.; Pan, C. Flexible Photodetector Arrays Based on Patterned  $\text{CH}_3\text{NH}_3\text{PbI}_{3-x}\text{Cl}_x$  Perovskite Film for Real-Time Photosensing and Imaging. *Adv. Mater.* **2019**, *31*, 1805913.

(16) Xia, K.; Wu, W.; Zhu, M.; Shen, X.; Yin, Z.; Wang, H.; Li, S.; Zhang, M.; Wang, H.; Lu, H.; Pan, A.; Pan, C.; Zhang, Y. CVD Growth of Perovskite/Graphene Films for High-Performance Flexible Image Sensor. *Sci. Bull.* **2020**, *65*, 343–349.

(17) Yang, Z.; Lu, J.; ZhuGe, M.; Cheng, Y.; Hu, J.; Li, F.; Qiao, S.; Zhang, Y.; Hu, G.; Yang, Q.; Peng, D.; Liu, K.; Pan, C. Controllable Growth of Aligned Monocrystalline  $\text{CsPbBr}_3$  Microwire Arrays for Piezoelectric-Induced Dynamic Modulation of Single-Mode Lasing. *Adv. Mater.* **2019**, *31*, 1900647.

(18) Li, F.; Lu, J.; Zhang, Q.; Peng, D.; Yang, Z.; Xu, Q.; Pan, C.; Pan, A.; Li, T.; Wang, R. Controlled Fabrication, Lasing Behavior and Excitonic Recombination Dynamics in Single Crystal  $\text{CH}_3\text{NH}_3\text{PbBr}_3$  Perovskite Cuboids. *Sci. Bull.* **2019**, *64*, 698–704.

(19) Qin, C.; Matsushima, T.; Potschavage, W.; J, J.; Sandanayaka, A. S. D.; Leyden, M.; Bencheikh, F.; Goushi, K.; Mathevet, F.; Heinrich, B.; Yumoto, G.; Kanemitsu, Y.; Adachi, C. Triplet Management for Efficient Perovskite Light-Emitting Diodes. *Nat. Photonics* **2020**, *14*, 70–75.

(20) Shen, Y.; Cheng, L.; Li, Y.; Li, W.; Chen, J. D.; Lee, S.; Tang, J. High-Efficiency Perovskite Light-Emitting Diodes with Synergetic Outcoupling Enhancement. *Adv. Mater.* **2019**, *31*, 1901517.

(21) Wang, S.; Li, L.; Weng, W.; Ji, C.; Liu, X.; Sun, Z.; Lin, W.; Hong, M.; Luo, J. Trilayered Lead Chloride Perovskite Ferroelectric Affording Self-Powered Visible-Blind Ultraviolet Photodetection with Large Zero-Bias Photocurrent. *J. Am. Chem. Soc.* **2020**, *142*, 55–59.

(22) Li, D.; Zhou, D.; Xu, W.; Chen, X.; Pan, G.; Zhou, X.; Ding, N.; Song, H. Plasmonic Photonic Crystals Induced Two-Order Fluorescence Enhancement of Blue Perovskite Nanocrystals and Its Application for High-Performance Flexible Ultraviolet Photodetectors. *Adv. Funct. Mater.* **2018**, *28*, 1804429.

(23) Gong, M.; Sakidja, R.; Goul, R.; Ewing, D.; Casper, M.; Stramel, A.; Elliot, A.; Wu, J. Z. High-Performance All-Inorganic  $\text{CsPbCl}_3$  Perovskite Nanocrystal Photodetectors with Superior Stability. *ACS Nano* **2019**, *13*, 1772–1783.

(24) Zhang, Y.; Liu, Y.; Xu, Z.; Ye, H.; Li, Q.; Hu, M.; Yang, Z.; Liu, S. Two-dimensional  $(\text{PEA})_2\text{PbBr}_4$  Perovskite Single Crystals for a

- High Performance UV-Detector. *J. Mater. Chem. C* **2019**, *7*, 1584–1591.
- (25) Adinolfi, V.; Ouellette, O.; Saidaminov, M. I.; Walters, G.; Abdelhady, A. L.; Bakr, O.; Sargent, E. Fast and Sensitive Solution-Processed Visible-Blind Perovskite UV Photodetectors. *Adv. Mater.* **2016**, *28*, 7264–7268.
- (26) Chen, Z.; Li, C.; Zhumekenov, A. A.; Zheng, X.; Yang, C.; Yang, H.; He, Y.; Turedi, B.; Mohammed, O. F.; Shen, L.; Bakr, O. M. Solution-Processed Visible-Blind Ultraviolet Photodetectors with Nanosecond Response Time and High Detectivity. *Adv. Opt. Mater.* **2019**, *7*, 1900506.
- (27) Shen, K.; Xu, H.; Li, X.; Guo, J.; Sathasivam, S.; Wang, M.; Ren, A.; Choy, K. L.; Parkin, I. P.; Guo, Z.; Wu, J. Flexible and Self-Powered Photodetector Arrays Based on All-Inorganic CsPbBr<sub>3</sub> Quantum Dots. *Adv. Mater.* **2020**, *32*, 2000004.
- (28) Tian, W.; Min, L.; Cao, F.; Li, L. Nested Inverse Opal Perovskite toward Superior Flexible and Self-Powered Photodetection Performance. *Adv. Mater.* **2020**, *32*, 1906974.
- (29) Leung, S.; Ho, K.; Kung, P.; Hsiao, V.; Alshareef, H.; Wang, Z.; He, J. A Self-Powered and Flexible Organometallic Halide Perovskite Photodetector with Very High Detectivity. *Adv. Mater.* **2018**, *30*, 1704611.
- (30) Ji, C.; Dey, D.; Peng, Y.; Liu, X.; Li, L.; Luo, J. Ferroelectricity-Driven Self-Powered Ultraviolet Photodetection with Strong Polarization Sensitivity in a Two-Dimensional Halide Hybrid Perovskite. *Angew. Chem., Int. Ed.* **2020**, *59*, 18933–18937.
- (31) Cao, F.; Tian, W.; Meng, L.; Wang, M.; Li, L. Ultrahigh-Performance Flexible and Self-Powered Photodetectors with Ferroelectric P(VDF-TrFE)/Perovskite Bulk Heterojunction. *Adv. Funct. Mater.* **2019**, *29*, 1808415.
- (32) Liao, W.; Zhang, Y.; Hu, C.; Mao, J.; Ye, H.; Li, P.; Huang, S. D.; Xiong, R. A Lead-Halide Perovskite Molecular Ferroelectric Semiconductor. *Nat. Commun.* **2015**, *6*, 7338.
- (33) Ji, C.; Wang, S.; Li, L.; Sun, Z.; Hong, M.; Luo, J. The First 2D Hybrid Perovskite Ferroelectric Showing Broadband White-Light Emission with High Color Rendering Index. *Adv. Funct. Mater.* **2019**, *29*, 1805038.
- (34) Wu, Z.; Ji, C.; Li, L.; Kong, J.; Sun, Z.; Zhao, S.; Wang, S.; Hong, M.; Luo, J. Alloying n-Butylamine into CsPbBr<sub>3</sub> to Give a Two-Dimensional Bilayered Perovskite Ferroelectric Material. *Angew. Chem., Int. Ed.* **2018**, *57*, 8140–8143.
- (35) Wang, B.; Zhu, Y.; Dong, J.; Jiang, J.; Wang, Q.; Li, S.; Wang, X. Self-Powered, Superior High Gain Silicon-Based Near-Infrared Photosensing for Low-Power Light Communication. *Nano Energy* **2020**, *70*, 104544.
- (36) Dai, Y.; Wang, X.; Peng, W.; Xu, C.; Wu, C.; Dong, K.; Liu, R.; Wang, Z. Self-Powered Si/CdS Flexible Photodetector with Broadband Response from 325 to 1550 nm Based on Pyro-Phototronic Effect: An Approach for Photosensing below Bandgap Energy. *Adv. Mater.* **2018**, *30*, 1705893.
- (37) Chang, Y.; Wang, J.; Wu, F.; Tian, W.; Zhai, W. Structural Design and Pyroelectric Property of SnS/CdS Heterojunctions Contrived for Low-Temperature Visible Photodetectors. *Adv. Funct. Mater.* **2020**, *30*, 2001450.
- (38) Wang, Y.; Zhu, L.; Feng, Y.; Wang, Z.; Wang, Z. Comprehensive Pyro-Phototronic Effect Enhanced Ultraviolet Detector with ZnO/Ag Schottky Junction. *Adv. Funct. Mater.* **2019**, *29*, 1807111.
- (39) Zhao, K.; Ouyang, B.; Bowen, C. R.; Yang, Y. Enhanced Photocurrent via Ferro-Pyro-Phototronic Effect in Ferroelectric BaTiO<sub>3</sub> Materials for a Self-Powered Flexible Photodetector System. *Nano Energy* **2020**, *77*, 105152.
- (40) Yang, Z.; Wang, H.; Guo, L.; Zhou, Q.; Gu, Y.; Li, F.; Qiao, S.; Pan, C.; Wang, S. A Self-Powered Photodetector Based on MAPbI<sub>3</sub> Single-Crystal Film/n-Si Heterojunction with Broadband Response Enhanced by Pyro-Phototronic and Piezo-Phototronic Effects. *Small* **2021**, *17*, 2101572.
- (41) Domanski, K.; Correa-Baena, J.; Mine, N.; Nazeeruddin, M.; Abate, A.; Saliba, M.; Tress, W.; Hagfeldt, A.; Gratzel, M. Not All That Glitters Is Gold: Metal-Migration-Induced Degradation in Perovskite Solar Cells. *ACS Nano* **2016**, *10*, 6306–6314.
- (42) Ming, W.; Yang, D.; Li, T.; Zhang, L.; Du, M. Formation and Diffusion of Metal Impurities in Perovskite Solar Cell Material CH<sub>3</sub>NH<sub>3</sub>PbI<sub>3</sub>: Implications on Solar Cell Degradation and Choice of Electrode. *Adv. Sci.* **2018**, *5*, 1700662.
- (43) Wu, S.; Chen, R.; Zhang, S.; Babu, B. H.; Yue, Y.; Zhu, H.; Yang, Z.; Chen, C.; Chen, W.; Huang, Y.; Fang, S.; Liu, T.; Han, L.; Chen, W. A Chemically Inert Bismuth Interlayer Enhances Long-Term Stability of Inverted Perovskite Solar Cells. *Nat. Commun.* **2019**, *10*, 1161.
- (44) Gao, Y.; Walters, G.; Qin, Y.; Chen, B.; Min, Y.; Seifitokaldani, A.; Sun, B.; Todorovic, P.; Saidaminov, M. I.; Lough, A.; Tongay, S.; Hoogland, S.; Sargent, E. H. Electro-Optic Modulation in Hybrid Metal Halide Perovskites. *Adv. Mater.* **2019**, *31*, 1808336.
- (45) Ma, N.; Zhang, K. W.; Yang, Y. Photovoltaic-Pyroelectric Coupled Effect Induced Electricity for Self-Powered Photodetector System. *Adv. Mater.* **2017**, *29*, 1703694.
- (46) Feng, Y.; Zhang, Y.; Wang, Y.; Wang, Z. Frequency Response Characteristics of Pyroelectric Effect in p-n Junction UV Detectors. *Nano Energy* **2018**, *54*, 429–436.
- (47) Dai, M.; Chen, H.; Feng, R.; Feng, W.; Hu, Y.; Yang, H.; Liu, G.; Chen, X.; Zhang, J.; Xu, C. Y.; Hu, P. A Dual-Band Multilayer InSe Self-Powered Photodetector with High Performance Induced by Surface Plasmon Resonance and a Symmetric Schottky Junction. *ACS Nano* **2018**, *12*, 8739–8747.
- (48) Zhang, Z.; Li, C.; Lu, Y.; Tong, X.; Liang, F.; Zhao, X.; Wu, D.; Xie, C.; Luo, L. Sensitive Deep Ultraviolet Photodetector and Image Sensor Composed of Inorganic Lead-Free Cs<sub>3</sub>Cu<sub>2</sub>I<sub>5</sub> Perovskite with Wide Bandgap. *J. Phys. Chem. Lett.* **2019**, *10*, 5343–5350.
- (49) Dai, M.; Chen, H.; Wang, F.; Hu, Y.; Wei, S.; Zhang, J.; Wang, Z.; Zhai, T.; Hu, P. Robust Piezo-Phototronic Effect in Multilayer gamma-InSe for High-Performance Self-Powered Flexible Photodetectors. *ACS Nano* **2019**, *13*, 7291–7299.
- (50) Li, Q.; van de Groep, J.; Wang, Y.; Kik, P. G.; Brongersma, M. Transparent Multispectral Photodetectors Mimicking the Human Visual System. *Nat. Commun.* **2019**, *10*, 4982.
- (51) Wang, Y.; Chiang, C.; Chang, C.; Maeda, H.; Fukui, N.; Wang, I.; Wen, C.; Lu, K.; Huang, S.; Jian, W.; Chen, C.; Tsukagoshi, K.; Nishihara, H. Two-Dimensional Bis(dithiolene)iron(II) Self-Powered UV Photodetectors with Ultrahigh Air Stability. *Adv. Sci.* **2021**, *8*, 2100564.
- (52) Ouyang, B.; Zhang, K.; Yang, Y. Photocurrent Polarity Controlled by Light Wavelength in Self-Powered ZnO Nanowires/SnS Photodetector System. *iScience* **2018**, *1*, 16–23.
- (53) Chen, J.; You, D.; Zhang, Y.; Zhang, T.; Yao, C.; Zhang, Q.; Li, M.; Lu, Y.; He, Y. Highly Sensitive and Tunable Self-Powered UV Photodetectors Driven Jointly by p-n Junction and Ferroelectric Polarization. *ACS Appl. Mater. Interfaces* **2020**, *12*, 53957–53965.